Quantifying Microenvironmental Forces in Engineered Tissue Models

By

Prerna Chordiya

B. Tech, National Institute of Technology Rourkela, India

Thesis
Submitted in partial fulfillment of the requirements for the Degree of Master of Science in the Graduate Program of Biomedical Engineering at Brown University

PROVIDENCE, RHODE ISLAND
MAY 2024

AUTHORIZATION TO LEND AND REPRODUCE THE THESIS

As the sole author of this thesis, I authorize Brown University to lend it to other institutions for the purpose of scholarly research.

Date _____ _____

Prerna Chordiya, Author

I further authorize Brown University to reproduce this thesis by photocopying or other means, in total or in part, at the request of other institutions or individuals, for the purpose of scholarly research.

Date _____

_____

Prerna Chordiya, Author

This thesis by Prerna Chordiya is accepted in its present form by the Institute of Biology, Engineering, and Medicine as satisfying the thesis requirements for the degree of Master of Science

Date _____ Signature: _____
Dr. Eric M Darling, Advisor

Date _____ Signature: _____
Dr. Michelle Dawson, Reader

Date _____ Signature: _____
Dr. Haneesh Kesari, Reader

Approved by the Graduate Council

Date _____ Signature: _____
Dr. Marissa Gray, Program Director

ACKNOWLEDGEMENTS

I would like to express my sincere gratitude to everyone who supported me throughout the completion of the thesis. First and foremost, I am deeply thankful to my advisor Dr. Eric Darling for their continuous guidance, valuable insights, and encouragement, which were instrumental in shaping this project. I am very grateful to Vera Fonseca for her constant support and guidance throughout this process. Her patience and kindness made a big difference as I worked through trainings, asked many questions, and dealt with technical challenges along the way.

I also extend my appreciation to my committee members for their constructive feedback and thoughtful suggestions. I am thankful to my lab members for their support, discussions, and for creating an encouraging environment. Funding for this research came from the National Science Foundation (CBET 1547819).

Special thanks to my family and friends for their unwavering encouragement and understanding during this journey.

Table of Contents

Table of Figures

Table of Tables

Abstract of Microenvironmental Forces in Engineered Tissue Models, Prerna Chordiya, ScM, Brown University, May 2026

Microenvironmental mechanical forces are key regulators of cellular behavior, yet their origin and modulation within three dimensional (3D) systems remains incompletely understood. In particular, the respective roles of cell-cell interactions and extracellular matrix (ECM) composition in governing these forces are not well defined. To address this, hypercompliant microparticles (HCMPs) were used to quantify microenvironmental mechanical parameters in two different models. First, dog bone system to investigate microenvironmental forces in early musculoskeletal regeneration. And second, cartilage spheroid model to evaluate changes in forces following enzymatic matrix degradation. Mechanical parameters like pressure, volume and elastic energy were analyzed to capture both system-level and sensor-level responses. The results indicate that while cellular interactions contribute to first generation force production as seen in the dog bone model, the ECM is essential for stabilizing and modulating the mechanical microenvironment. Matrix degradation leads to measurable alterations in microenvironmental mechanical states, highlighting the role of ECM composition in regulating for distribution. Together, this study provides a framework for directly measuring and interpreting microenvironmental forces in 3D systems, with implications for the disease modeling and tissue engineering.

CHAPTER 1:

INTRODUCTION

Mechanical environment of living tissues plays fundamental role in regulating cellular behavior, tissue development, and disease progression[1-3]. Cells continuously exert as well as respond to physical cues such as tension, compression, and matrix stiffness, translating these signals into biochemical responses through mechanotransduction pathways[4-5]. Especially, musculoskeletal tissues that is subjected to dynamically evolving environment tend to make cells hypersensitive to the physical cues[6]. Investigating these forces will have significant application in tissue engineering, disease modeling as well as wound healing[7-9]. Knowledge remains limited because current techniques for quantifying mechanical stimuli often inadvertently alter and influence cell structure and behavior. Existing methods include traction force microscopy (TFM) and micropillars which though work well for isolated cells but lack suitability for cell dense structures[10-12]. Furthermore, these techniques are performed in 2D and are difficult to translate into three dimensional cultures that mimic physiology for several biological systems.

Another explored method for mechanical sensing is deformable microparticles (MPs) which have been used as an in-situ force sensor[13]. Previous studies have largely focused on general observations of forces in 2D culture or around the peripheries. They also used much stiffer or much larger than cells which limits its accuracy and sensitivity. Labs including ours have created hyper compliant microparticles (HCMPs) from polyacrylamide via an inversion emulsion process. These HCMPs possess tunable properties with size and elastic modulus around the same range as cells. Previous work of our group quantified the forces present in self-assembled adipose-derived stem cell spheroid using customized HCMPs[14]. Recently, our group

also reported the effect of HCMP's physical characteristics on mechanical measurements and uncovered that HCMPs with diameter $\geq 20\ \mu m$ and elastic modulus ~250 Pa had greatest measurement resolution and sensitivity in 3D spheroid model[15].

The aim of the study is to utilize HCMPs to investigate the evolution of microenvironmental forces within two distinct 3D model systems. The first being dog bone model, that previously have been used as a model for uniaxial tension relevant to musculoskeletal tissues such as tendons and ligaments. The second is a 3D spheroid model of self-assembled chondrogenic progenitor cells, which provides a physiologically relevant platform to study compressive forces and their evolution within a cartilage-like microenvironment.

Through the integration of these models and methodologies, this work aims to provide deeper insights of how mechanical microenvironment evolve in response to structural and compositional changes.

CHAPTER 2:

MICROENVIRONMENTAL FORCES IN

EARLY MUSCULOSKELETAL TISSUE FORMATION

2.1. Introduction

Mechanical loading in musculoskeletal tissues such as ligaments and tendons is predominantly tensile, where cells exist within highly aligned, load bearing environments and continuously generate and respond to forces[16-17]. The ECM, particularly collagen alignment contributes significantly to achieving tensile strength[19]. In addition to ECM, fibroblasts and tenocytes are also critical in maintaining tissue mechanics through active remodeling[19]. However, existing literature has extensively characterized role of collagen fiber alignment in tensile behavior, the contribution of cells themselves as force generating units remains less understood.

Self-assembled dog bone microtissues have emerged as a powerful model system to study uniaxial tension in engineered tissues[20]. Driven by cell-mediated contractility and geometric constraint, these constructs spontaneously organize into aligned structures that generate intrinsic tensile strength along a defined axis. This makes them particularly relevant for modeling native musculoskeletal tissues, where structural anisotropy and tension-driven organization are critical to function. Normal human fibroblasts were used to seed dog bone microtissues as they take 3 to 7 days to produce detectable ECM and 7 to 14 days for mature ECM deposition[21], thereby leading to cell-driven forces to be more prominent. Previous work from our lab has successfully utilized this system to investigate microenvironmental forces and

demonstrated feasibility of integrating deformable microparticle as embedded force sensors within the constructs.

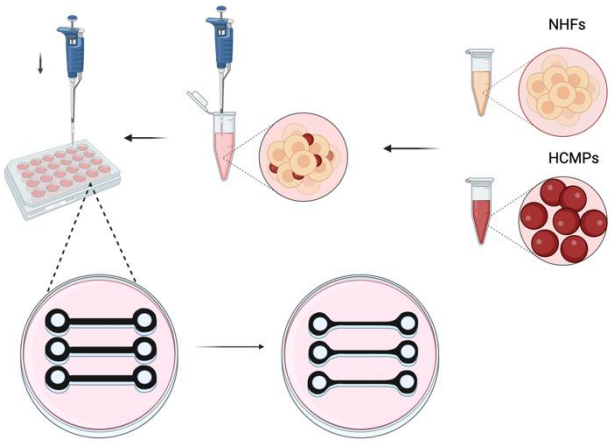

Figure 1: Visual representation of NHF-dog bone microtissue seeding. (Biorender)

However, a key limitation in prior implementation lies in the heterogeneous size distribution of these HCMPs. Non-uniform sizes can affect deformation responses, thereby limiting the ability to reliably compare force magnitudes across regions and timepoints. To address this, the present study builds upon this established platform by introducing a more monodisperse HCMPs.

2.2. Methods

2.2.1. HCMPs fabrication and characterization

The force sensors used in this study were polyacrylamide HCMPs fabricated as described[14,22-23]. Monodispersed sensor batch was created using microfluidic droplet generator using aqueous discontinuous phase (polyacrylamide precursor solution) and an oil continuous phase (1-octadecene with 2.5% Hypermer SP6). To target a stiffness of 300 Pa, a polyacrylamide formation of 4% acrylamide and 0.08% bisacrylamide was used. 8% triphenylmethane Sharpie dye (640 nm excitation, 670 nm emission), 0.1% ammonium persulfate (APS), and 0.1% lithium phenyl-2,4,6-trimethylbenzoylphosphinate (LAP) were also included in the precursor solution. The target sensor size was 40 μm. Microdroplets were polumerized on a UV curing chip and then washed three times with 0.1% Triton X-100 and three times with deionized (DI) water. Sensors were allowed to fully hydrate in DI water away from light before use.

After fabrication, the size and elastic modulus was characterized for a sample of each batch. Size was determined in ImageJ with the Particle Analyzer function, and elastic modulus was measured using force-indentation curves collected on an atomic force microscope with a 5-mm spherically tipped indenter (nominal k ~0.03 N/m) as previously described[24].

2.2.2. Cell culture

Experiments used NHFs between passage 7 to 9. Cells were cultured in medium containing Dulbecco's Modified Eagle Medium with high glucose (DMEM-hg), 10% fetal bovine serum, and 1% penicillin-streptomycin and proliferated at 37℃ and 5% CO_2.

2.2.3. Dog bone mold preparation

Microtissue wells were prepared with 3D printed mold. The dog bone wells consist of two tori with diameter of 800 μm set 6mm apart and connected by a 400 μm wide connecting rod. 600 μL of 3% agarose was placed in each well followed by the 3D printed mold, and the agarose was then cooled to form three dog bone microtissue wells within each well. Microtissue wells were acclimated at least thrice in base medium with 1% penicillin streptomycin. Wells with two intact tori and no damage to the dog bone structure were used for seeding.

2.2.4. Dog bone microtissue seeding

80-90% confluent flasks were rinsed with PBS and lifted using trypsin/EDTA and incubated for 6 minutes at 37℃ and 5% CO_2. Culture medium was added to neutralize trypsin, and the cells were then centrifuged at 400g for 5 minutes, resuspended in culture media and counted using hemocytometer. The microtissue wells were seeded with ~600,000 cells/dog bone for based on previous work that determined suitable seeding concentration to ensure microtissue remained intact during the experimental period. 3-20 force sensors were seeded per dog bone to avoid overcrowding and affect the tissue architecture. After seeding, the well plate was left to sit at room temperature under biosafety cabinet for 30 minutes to allow the cells to settle and reduce loss of cells or sensors to other regions. Well plate was then transferred into an incubator at 37℃ and 5% CO_2.

2.2.5. Image collection

At timepoints 4h, 8h and 24h, 2D images of the dog bones were taken using 10X objective in brightfield and Cy5 (628 nm excitation, 685 nm emission). Manual imaging mode was used to capture images of dog bone microtissue with no overlap setting to enable proper

image stitching. Cy5 images were captured at 2-4 different z-heights per dog bone to capture as many sensors as possible. Exposure and power settings were adjusted for different filters. The x-y resolution (0.6446 μm /pixel) was recorded for further image processing.

2.2.6. Image processing

To calculate microenvironmental measurements, sensor images were extracted from stitched Cy5 files through MATLAB, followed by computational analysis in Mathematica. The MATLAB script utilized Otsu thresholding to convert images at different z-levels into one binary map, and the x- and y- coordinates of the sensor centroids were then computed. The code created a virtual Time0 particle with a diameter equal to the measured average of the monodispersed sensor lot. The resulting output was a pair of folders for each sensor with binary images of the undeformed (Time0) and deformed (Time1) states. A virtual Time0 was used in this study based on previous findings that between matched real and virtual Time0 sensors, there were no significant differences in average pressure or elastic energy measurements for soft sensor[15].

A Wolfram Mathematica program developed specifically for 2D image analysis was the used to compute mechanical parameters: average pressure, elastic energy, and elastic energy density[14]. The program enables parallel processing of image data to extract mechanical measurements using assumptions of spherical symmetry and continuum mechanics. Computational parameters used to run the Mathematica program are listed in *Table 1*. The pixel ratio was calculated once using image metadata on dimensions in pixels and μm, as all images were acquired with the same resolution. For reported average pressure values, negative values represent compressive acting on the sensors while positive values represent outward tensile forces. Force measurements were calculated using average pressure and the area of the circle

with radius equal to sensor minor axis to analyze force acting in the direction of the major axis. MATLAB scripts were then used to overlay the computed forces and their orientations onto the stitched images, followed by downstream analysis comparing mechanical parameters and geometric measurements of sensor elongation and orientation over time and in different regions of the dog bone.

Table 1: Parameter palette used to run Wolfram Mathematica program for dog bone microtissue

Binarize Threshold	0.06
Edge Detect Scale	2
Pixel ratio (μm/pixel)	0.6446
Young's modulus (Pa)	250
Poisson's ratio	0.443

2.2.7. Statistical Analysis

All statistical analyses were performed using R studio and GraphPad Prism 11. Outliers in the data were identified using the ROUT method with Q=1% and removed before analyses. Normal distribution for continuous variables was tested using Kolmogorov-Smirnov test, histograms and Q-Q plots. One-way ANOVA with Dunn's post hoc test was performed on nonparametric variables. Tukey box and whisker plots were used to visualize data. Associations with p values < 0.05 were considered statistically significant. Graphs were created using GraphPad prism 11.

2.3. Results

Imaging data was collected for 29 NHF-seeded dog bones at 4h, 8h, and 24h timepoints. The same force sensor lot (33 μm diameter particle with elastic modulus of 250 Pa) was used for all experiments.

2.3.1. Morphology of NHFs in dog bone

Figure 2 shows brightfield images of NHF microtissue at 4h, 8h and 24h. Over time, microtissue exhibited compaction, resulting in a more condensed and structurally tighter morphology. At 24h, it was more pronounced in the neck region, with comparatively less but noticeable tightening around ring region.

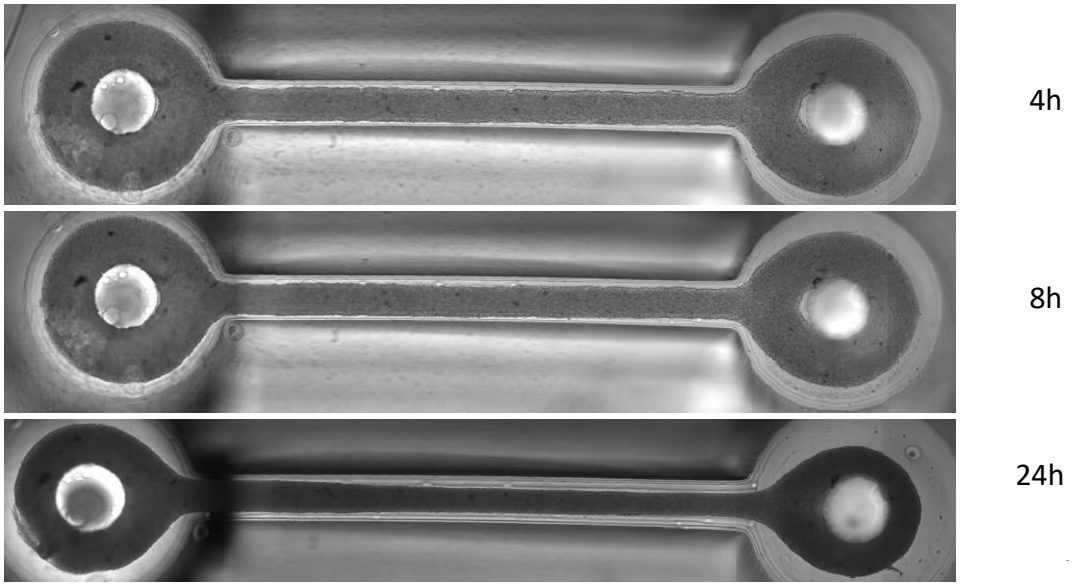

Figure 2: Brightfield stitched images of dog bone microtissues at 4h, 8h and 24h timepoint.

2.3.2. Mechanical Parameters for NHF-seeded dog bones

2.3.2.1. Combined force maps

Force sensors from all 29 NHF dog bones were combined for each timepoint using coordinates calculated relative to the center of the left post. Average pressure across all time points was found be around 50-550 Pa (*Figure 3*). The color of the sensors indicates the average pressure experienced and the lines indicate the range of elongation. Outliers were removed from further analysis.

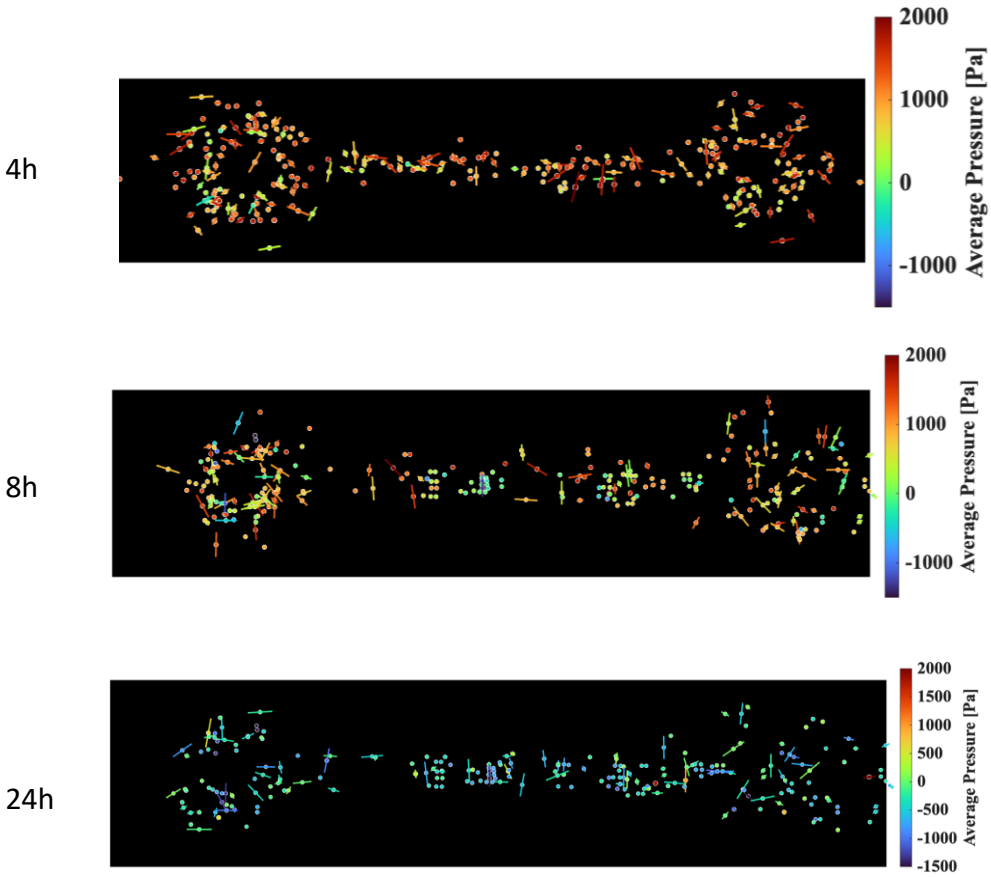

Figure 3: Combined force maps at 4h, 8h and 24h timepoint.

2.3.2.2. Parameter by region

For each timepoints, mechanical parameters like average pressure, force, and elastic energy density were calculated for the neck, neck-ring interface and ring regions at a single timepoint (*Figure 4*). No significant pressure and force differences were observed between any regions across all timepoints. At 8h and 24h, no changes in elastic energy density were observed across all regions, whereas at 4h it was found to be significantly higher in ring region compared to neck-ring interface ($p<0.05$).

2.3.2.3. Parameter changes over time

All three parameters were compared for each region at all three timepoints (*Figure 5*) to understand the change in the mechanical behavior based on the location. While average pressure, elastic energy density and force were consistent across time in each region, elastic energy density in neck and ring region was lower at 8h compared to 4h ($p<0.05$). Elastic energy density also increased in neck region in 24h compared to 8h ($p<0.01$).

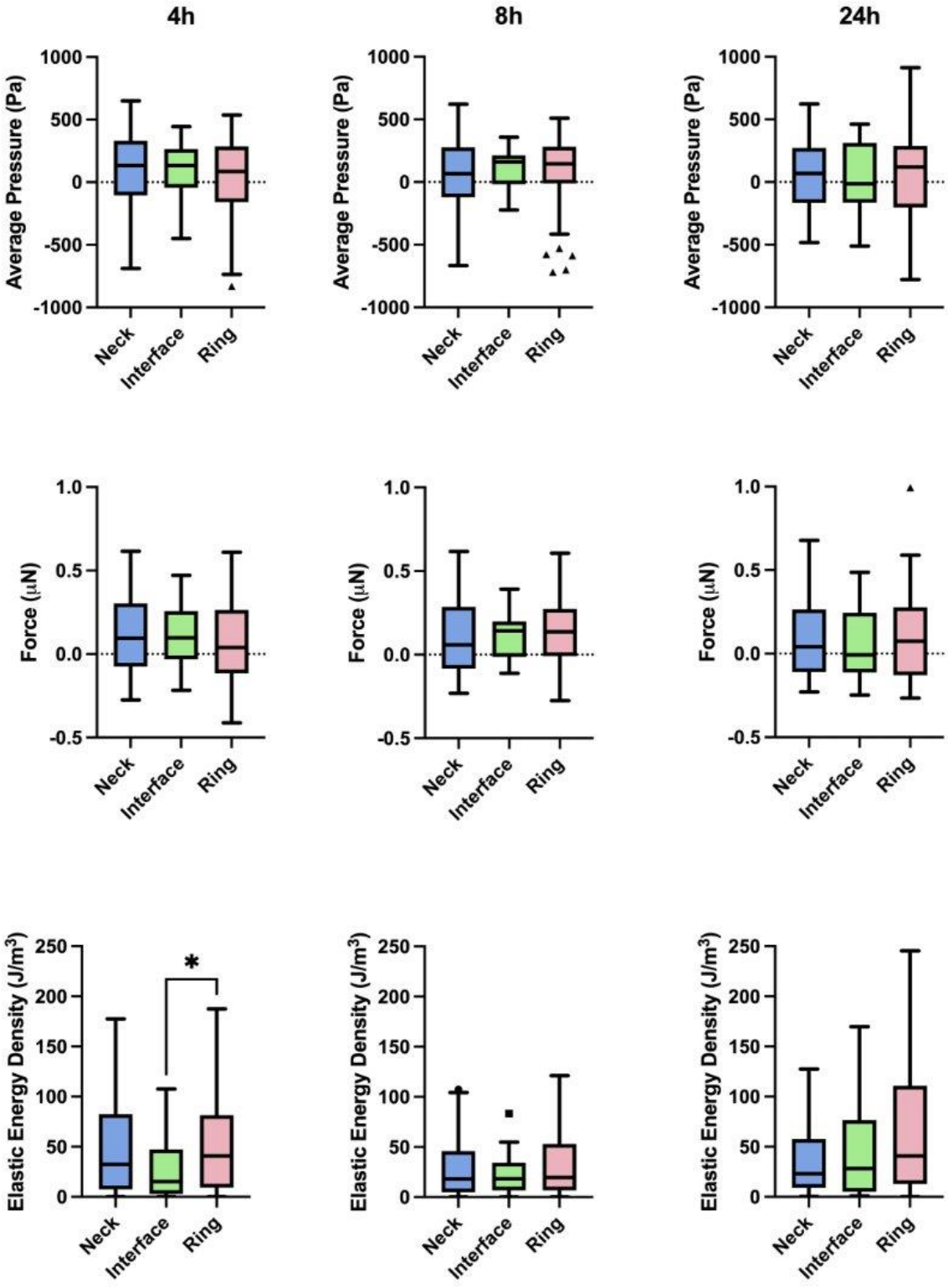

*Figure 4: Average Pressure (Pa), force (μN), and elastic energy density (J/m^3) measurements in the neck, neck-ring interface, and ring regions of NHF-seeded dog bone microtissues for 4h, 8h and 24h timepoint. *p<0.05, **p<0.01, ***p<0.001, ****p<0.0001*

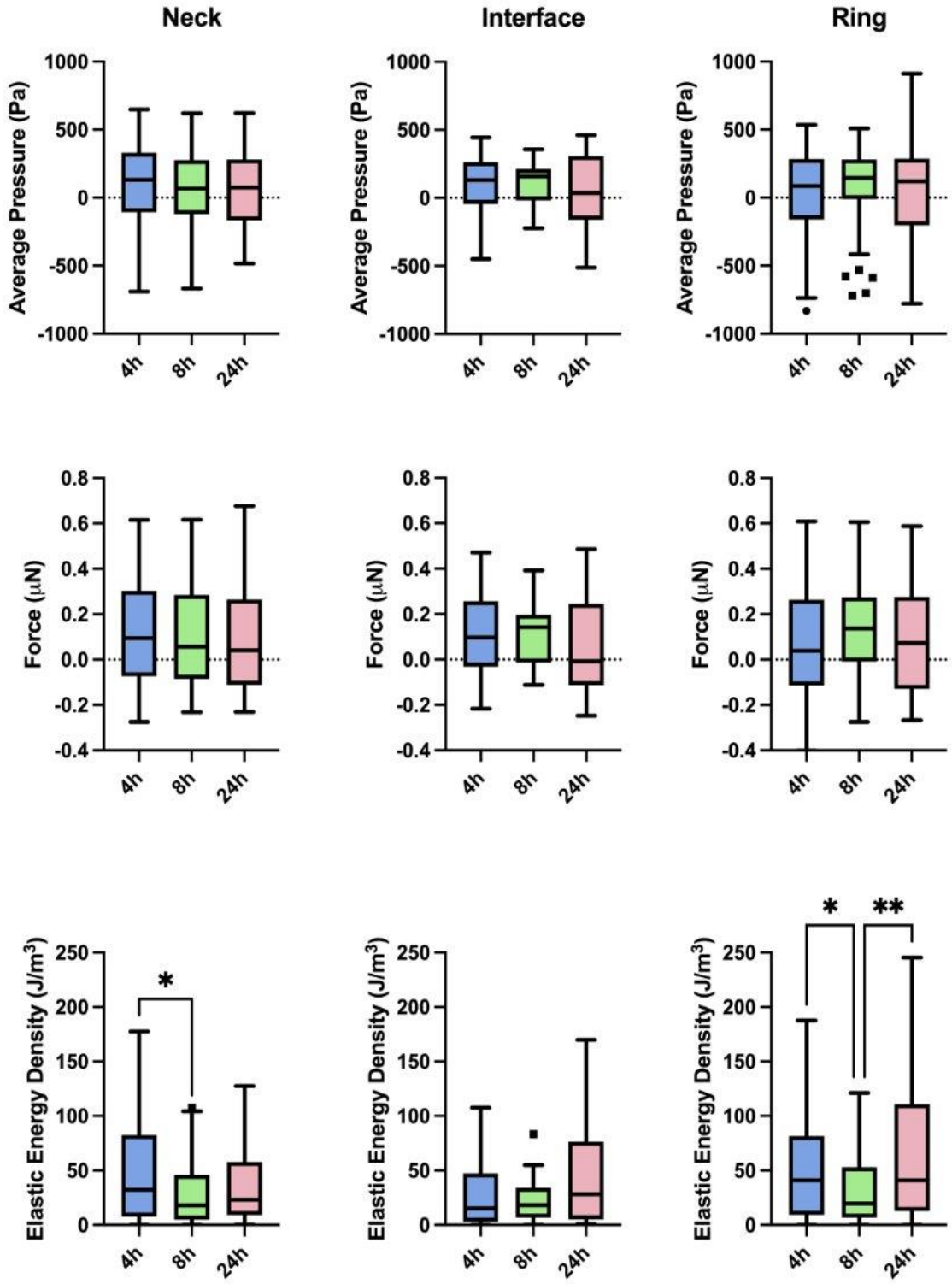

*Figure 5: Average Pressure (Pa), force (μN), and elastic energy density (J/m^3) measurements at 4h, 8h, and 24h for each region (neck, neck-ring interface, ring) of NHF-seeded dog bone microtissues. *p<0.05, **p<0.01, ***p<0.001, ****p<0.0001*

2.3.2.4. Sensor orientation and elongation

We hypothesized that sensors in the neck region would be horizontally oriented and sensors in the ring regions would be tangentially oriented to the post due to possible hoop stress according to finite element models[20]. To test this hypothesis, we measured degrees from horizontal of sensor major axes in neck region and deviation of sensor major axes from the tangent of the post for ring regions. As deviations could from the horizontal and tangent could result in either positive or negatives angles, absolute values were used to represent the measurements. There were no significant differences between degrees from horizontal or deviation from tangent measurements (*Figure 6*).

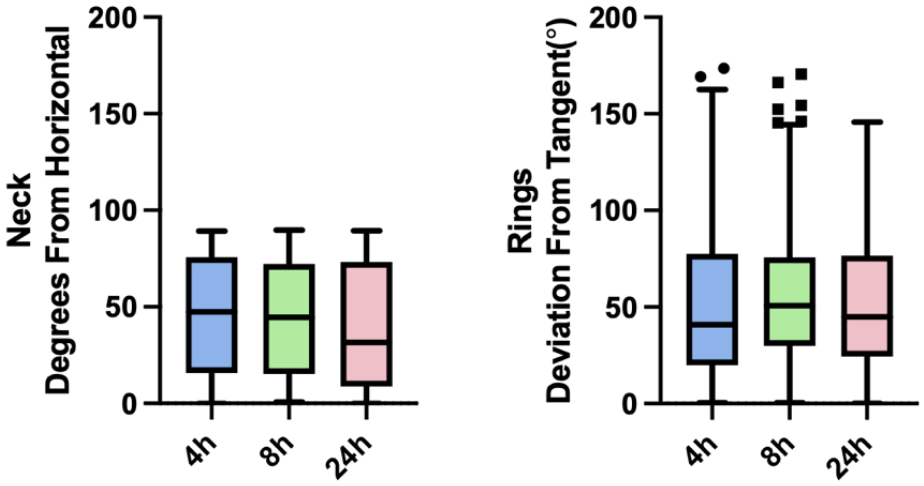

Figure 6: Absolute value of degrees from horizontal measurements in the neck region and degrees of deviation from tangent measurements in the rings at 4h, 8h, and 24h for NHF-seeded dog bone microtissues.

Changes in sensor's major-to-minor axis ratio over times in each region. Though major-to-minor axis ratios were significantly lower at 8h compared to 4h in all three regions, that might not be translatable into biological significance (*Figure 7*).

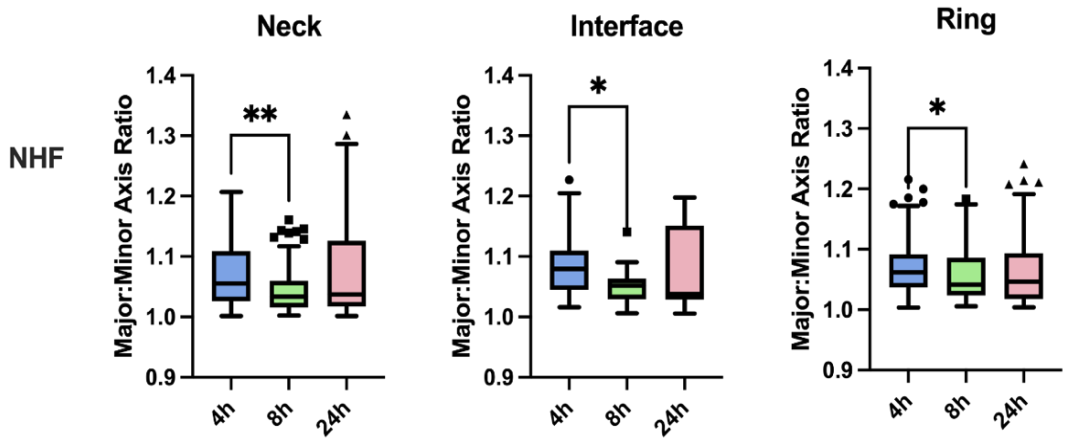

*Figure 7: Sensor major-to-minor axis ratio at 4h, 8h, and 24h for each region of NHF-seeded dog bone microtissues. *p<0.05, **p<0.01, ***p<0.001, ****p<0.0001*

2.4. Discussion

This study quantifies microenvironmental forces in *in vitro* model for early musculoskeletal tissue condensation. It provides insight on changes in magnitude and direction of mechanical parameters in different regions of microtissue over time.

Average pressure measurements indicated the presence of tensile forces primarily that aligns with our hypothesis that cells may also play a role in imparting tensile behavior. Some sensors in combined force sensor map appear to be outside of the microtissue, it could be due to variability in tissue condensation. In addition, image data was captured for around 300 force sensors to reduce error.

Across time and regions, average pressure, forces and elastic energy remained within the same range demonstrating no significant increase or decrease. This likely reflects the establishment of an early cell-dominated mechanical steady state. At these early timepoints, extracellular matrix deposition remains limited and thereby lacking structural organization to facilitate long-range force transmission[25]. As a result, while cells can generate little tensile forces, the absence of a mature and aligned collagen network likely constrains further increase in average pressure and force at 8h and 24h timepoints.

In addition to relatively stable tensile behavior, a compressive component was also observed across all timepoints (negative average pressure) in *Figure 4,* could be due to fibroblasts ability rapidly generate contractile forces through actomyosin activity and cell-cell interactions[26-27]. In absence of ECM forces remain locally distributed and can give rise to regions of inward compaction.

Sensor orientation in neck and ring regions did not significantly differ over time in NHF microtissue. Similarly, measurements of sensor elongation remained consistent over time in all three regions for NHF microtissues which was consistent with our hypotheses.

Limitation of our study is that the 24h timepoint could be too early to fully capture the role of cells in driving mechanical properties. 24h was used as the last timepoint as we aimed for early condensation process. And because the microtissue experienced failure around 48h timepoint. Furthermore, increasing seeding density to prolong structural stability led to decreased cell viability due to overcrowding. Another limitation of this study was in the imaging system and processing. In some cases, sensors that were out of focus were still identified as being in focus, introducing potential error in the measurements.

Previous work included microtissues containing 50-100 sensors. However, to eliminate the possibility of high amounts of sensors contributing to failure, this study reduced the number of sensors to less than 20 sensors per microtissue. Despite this reduction, failure was still observed for majority of the microtissues around 48h. As a result, the analysis was constrained to early timepoint. Further experimentations could benefit from the use of serum-free media to enable longer term assessment. Future studies could leverage this platform by incorporating force sensors into microtissues with more mature ECM to characterize the evolution of mechanical parameters in systems where both cellular and matrix composition is present. In parallel, decellularized constructs could be employed to isolate matrix-driven forces, providing a means to decouple and quantitatively compare cell-mediated and matrix-mediated mechanical measurements.

Together, these results highlight a distinct early-stage mechanical regime in which cells themselves act as the primary drivers of microenvironmental forces.

CHAPTER 3:

MICROENVIRONMENTAL FORCE CHANGES IN CARTILAGE TISSUE MODEL UPON MATRIX DEGRADATION

3.1. Introduction

Chondrocytes are the primary cells responsible for the formation of cartilage extracellular matrix[28]. These cells in oxygen-poor or hypoxic environment predominantly produce proteoglycans and collagen, which enables ECM to retain large amounts of water. This is essential for cartilage's flexibility and viscoelasticity[29-30].

Despite their importance, maintaining chondrocyte functionality *in vitro* within a physiologically relevant environment remains a significant challenge in cartilage tissue engineering[31]. Existing approaches to recreate cartilage-like systems are often limited by restricted tissue availability, low cell numbers, slow proliferation rates, and phenotypic instability during culture[32]. These limitations hinder the ability to accurately model the complex interplay between matrix composition, cellular behavior, and mechanical function in cartilage.

From a mechanical perspective, cartilage operates within a predominantly compressive environment, when its load-bearing capacity is largely governed by the presence of sulfated glycosaminoglycans (sGAG)[33-34]. sGAG are known to attract water, generating osmotic swelling pressure, thereby serving as shock absorbers and providing compressive resilience to cartilage tissue[35-36]. Chondroitinase ABC (C-ABC) an enzyme that degrades sGAG and in prior studies have been used in ECM remodeling, enhancing collagen maturation and hence improving structural and mechanical properties of engineered cartilage and meniscus tissues[37-

[40]. Prior studies have shown that early application of C-ABC (t = 1wk) was beneficial in enhancing tensile properties of cartilage construct[37].

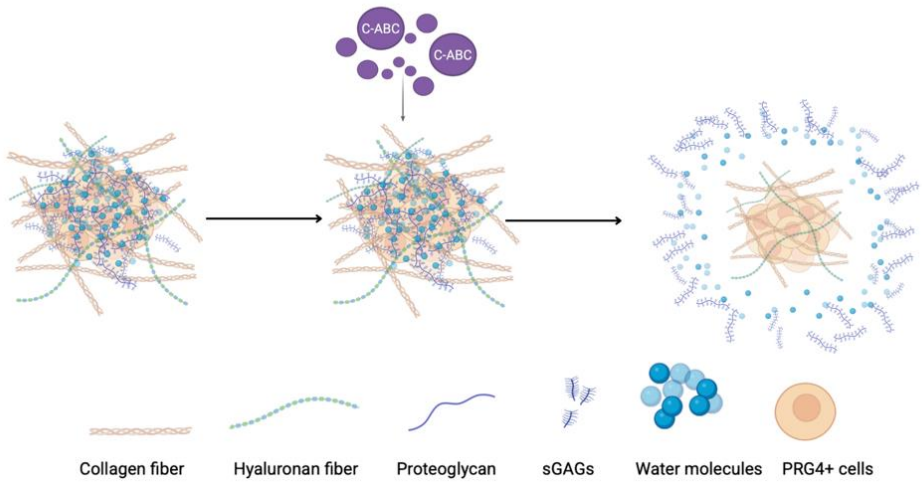

Figure 8: Graphical representation of spheroid microenvironment (Biorender).

Three-dimensional spheroid models provide a promising platform to study these phenomena in a controlled yet biologically relevant microenvironment. Prior work from our lab has demonstrated the use of ASC spheroids to investigate microenvironmental forces using HCMPs, establishing the feasibility of capturing local mechanical changes within cell spheroids[14]. Preliminary studies have also explored mechanical changes in PRG4+ expressing cells that possess cartilage-specific phenotypes[41]. We hypothesize that the temporary depletion of sGAG using C-ABC would release the water content and thereby lowering the osmotic pressure in the tissue microenvironment.

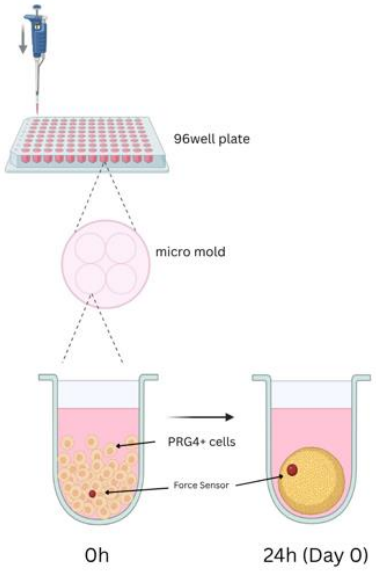

Figure 9: Representation of PRG4+ spheroid seeding (Biorender)

3.2. Methods

3.2.1. HCMP fabrication and characterization

The force sensors used in this study were polyacrylamide HCMPs fabricated as described. Monodispersed sensor batch was created using microfluidic droplet generator using aqueous discontinuous phase (polyacrylamide precursor solution) and an oil continuous phase (1-octadecene with 2.5% Hypermer SP6). To target a stiffness of 300 Pa, a polyacrylamide formation of 4% acrylamide and 0.08% bisacrylamide was used. 8% triphenylmethane Sharpie dye (640 nm excitation, 670 nm emission), 0.1% ammonium persulfate (APS), and 0.1% lithium phenyl-2,4,6-trimethylbenzoylphosphinate (LAP) were also included in the precursor solution. The target sensor size was 30 μm. Microdroplets were polumerized on a UV curing chip and then washed three times with 0.1% Triton X-100 and three times with deionized (DI) water. Sensors were allowed to fully hydrate in DI water away from light before use.

After fabrication, the size and elastic modulus was characterized for a sample of each batch. Size was determined in ImageJ with the Particle Analyzer function, and elastic modulus was measured using force-indentation curves collected on an atomic force microscope with a 5-mm spherically tipped indenter (nominal k ~0.03 N/m) as previously described (Darling et al, 2006). Resulting sensors were found to have 18 μm diameter and elastic modulus of 300 Pa.

3.2.2. Cell culture

PRG4+ cells in culture media consisting of DMEM/F12, 10% FBS (placeholder) and 1% penicillin-streptomycin (placeholder) were cultured at 37℃ and 5% CO_2. At 80-90% confluence, the cell monolayer was treated with trypsin and incubated for 5 minutes to detach them from the flask surface. Trypsin consisting of cells was then neutralized using culture media

and centrifuged at 400g for 5 minutes. Cells were resuspended in culture media and counted using hemocytometer before the experiment.

3.2.3. Microarray preparation

Two different types of microtissue array were used. One in 96 well plate and other in 24 well plate. 96 well array was used for microenvironmental force measurement whereas for all biochemical assays and histology 24 well plate array was used.

3.2.3.1. 96 well array

To prepare 96well array, 2% sterile agarose solution was prepared. Using multichannel pipette 140uL of molten agarose was dispensed into each well and stamped with the mold. The mold was left on for 15 mins to solidify the agarose to form four conical microwells. Following solidification, the mold was carefully removed, and the hydrogels were acclimated using DMEM/F12 supplemented with 1% penicillin-streptomycin at 37C prior to seeding.

3.2.3.2. 24 well array

To prepare 24 well array, 100μL of 3%csterile agarose is added to the mold and glass slides are placed on top of it for 15 mins. The slide is then taken off and the solidified is carefully removed from the mold and placed in the 24 well. The hydrogels were acclimated using DMEM/F12 supplemented with 1% penicillin-streptomycin at 37C prior to seeding.

3.2.4. Microtissue seeding

3.2.4.1. 96 well microtissue

For 96 well microarray, 10uL aliquot of cells and HCMP suspension (1:1) was pipetted into each well to form four spheroids each composed of 6500 cells in addition to ~1-2 HCMPs.

To assist spheroid formation seeded plates were centrifuged for 5 mins at 400g. Following centrifugation, each well was given 130 μL of growth media. 24h post seeding, once the spheroids are compact growth media was replaced with chondrogenic medium

3.2.4.2. 24 well microtissue

For 24 well microarray, 50 μL of cell suspension was added to the loading deck of each hydrogel and kept steady for 30mins to facilitate spheroid formation. After 30mins, growth media was gently added to the hydrogels. 24h post seeding, growth media was replaced with chondrogenic media.

3.2.5. Chondro-Induction media:

Chondro-induction media comprised of DMEM High glucose, 10% FBS, 0.5% 2ug/mL TGF beta 1, 0.1% 50ug/mL ascorbate-2-phosphate, 1% 10 μM dexamethasone, 1% Insulin and 1% Antibiotic/antimycotic.

3.2.6. Chondroitinase-ABC treatment:

At timepoints t = 1 day and t = 5 day, spheroids were treated with Chondroitinase-ABC (C-ABC). The protocol for the treatment was followed as mentioned[37]. 2U/mL C-ABC and 0.05M acetate activator in chondrogenic medium for 4h at 37℃.

3.2.7. Biochemical Assays

At 1st, 5th and 14th day spheroids were treated with C-ABC and fixed in 3.7% paraformaldehyde. Samples containing approximately 30 spheroids each for control and treatment were digested with papain at 65℃ for 48 hours. Microplate reader (Cytation 5) was used to quantify sGAG, total collagen, and DNA content from papain digested samples. sGAG

amount was quantified via dimethylmethylene blue (DMMB) assay and measured at 525. Total collagen content was measured by a hydroxyproline assay and measured at 550 nm. DNA content was quantified using the Quant-iT Picogreen dsDNA Assay Kit and read at 480 nm excitation and 520 nm emission. A standard curve was used to calculate sGAG, total collagen and DNA amounts per spheroid.

3.2.8. Image collection:

Spheroids images were taken at different timepoints using the inverted digital widefield microscope (Cytation 5) with 10X objective in brightfield and Cy5 (628 nm excitation, 685 nm emission). Exposure and power settings were adjusted for different filters. The x-y resolution (0.6446 μm /pixel) was recorded for further image processing.

3.2.9. Image processing/ acquisition

To calculate microenvironmental measurements, sensor images were extracted through MATLAB, followed by computational analysis in Mathematica. The MATLAB script utilized Otsu thresholding to convert images into a binary map, and the x- and y- coordinates of the sensor centroids were then computed. The code created a virtual Time0 particle with a diameter equal to the measured average of the monodispersed sensor lot. The resulting output was a pair of folders for each sensor with binary images of the undeformed (Time0) and deformed (Time1) states. A virtual Time0 was used in this study based on previous findings that between matched real and virtual Time0 sensors, there were no significant differences in average pressure or elastic energy measurements for soft sensor.

A Wolfram Mathematica program developed specifically for 2D image analysis was the used to compute mechanical parameters: average pressure, elastic energy, and elastic energy

density. The program enables parallel processing of image data to extract mechanical measurements using assumptions of spherical symmetry and continuum mechanics. Computational parameters used to run the Mathematica program are listed in *Table 2*. The pixel ratio was calculated once using image metadata on dimensions in pixels and μm, as all images were acquired with the same resolution. For reported average pressure values, negative values represent compressive acting on the sensors while positive values represent outward tensile forces.

Table 2: Parameter palette used to run Wolfram Mathematica program for spheroid microtissue

Binarize Threshold	0.06
Edge Detect Scale	2
Pixel ratio (μm/pixel)	0.6446
Young's modulus (Pa)	300
Poisson's ratio	0.443

3.2.10 Percentage change for each sensor

The percentage change in mechanical parameters of each sensor was calculated using the formula:

$$Percentage\ change = \frac{(After\ treatment\ value - Before\ treatment\ value)}{|Before\ treatment\ value|} * 100$$

3.2.11 Statistical analysis

All statistical analyses were performed using R studio and GraphPad Prism 11. Outliers in the data were identified using the ROUT method with Q=1% and removed before analyses.

Normal distribution for continuous variables was tested using Shapiro Wilk test, histograms and Q-Q plots. Two-way Anova and multiple comparison tests were performed for each variable. Tukey box and whisker plots were used to visualize data. Associations with p values < 0.05 were considered statistically significant. Graphs were created using GraphPad prism 11.

3.3. Results

3.3.1. PRG4+ spheroids in chondrogenic media

3.3.1.1. PRG4 morphology

PRG4 cells (~6500/spheroids) were seeded into non-adhesive agarose microwells and were allowed to self-assemble into spheroids. Prior experimentation has showed that spheroids can be formed within 12-13h of seeding. At 24h post seeding, growth media was replaced with chondrogenic media, and spheroids were allowed to grow. Spheroids were imaged daily following the spheroid. Day 0 (24 h post seeding) was defined as the timepoint immediately prior to media replacement with chondrogenic medium (*Figure 10*). Average diameter across spheroids was found to be around 220 μm.

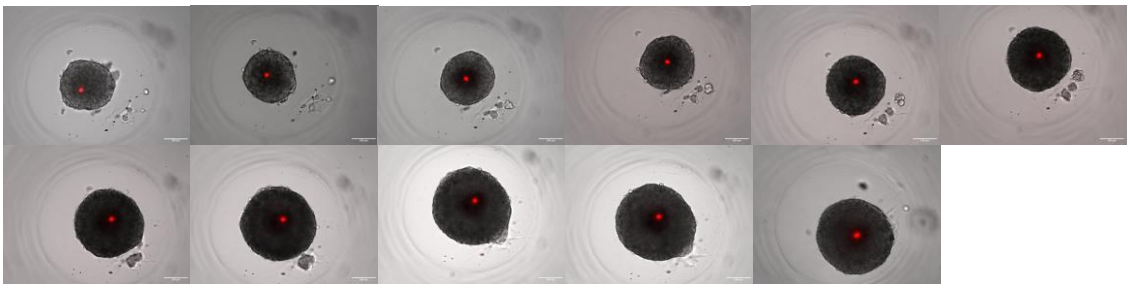

Figure 10: Representative imaging of PRG4+ spheroids containing sensors tracked longitudinally from Day 0 to Day 10. (Top left to right: Day 0 to Day 5, Bottom left to right: Day 6 to Day 10)

3.3.1.2. Average pressure in PRG4 spheroids in growth media and chondrogenic media

Average pressure before and after changing the growth media (N = 120) to chondrogenic media (N = 120) was measured to rule out possibility that any observed pressure changes were caused due to media switch. *Figure 11* shows the average pressure of the sensors in growth media (Day 0) and chondrogenic media (Day 1) for 24h.

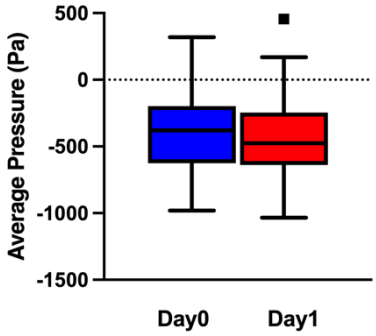

Figure 11: Average Pressure (Pa) of spheroids in growth media and chondrogenic media for 24h.

3.3.2. Quantification of extracellular matrix

To assess the extent of ECM, particularly sGAG degradation, and confirm the effect of C-ABC treatment, biochemical assays were performed to quantify sGAG, collagen, and DNA content within the spheroids. *Figure 12* shows sGAG, total collagen and DNA per sample for Day 1, Day 5 and Day 14 C-ABC treated and untreated spheroids. No significant change in total collagen or DNA per sample was found for either of the treated spheroids at either timepoints. Day 5 treated spheroids had significantly lower amount of sGAG compared to untreated spheroids (p=0.0097), while no significant change was observed in sGAG amount for Day 0 and Day 14 treated spheroids.

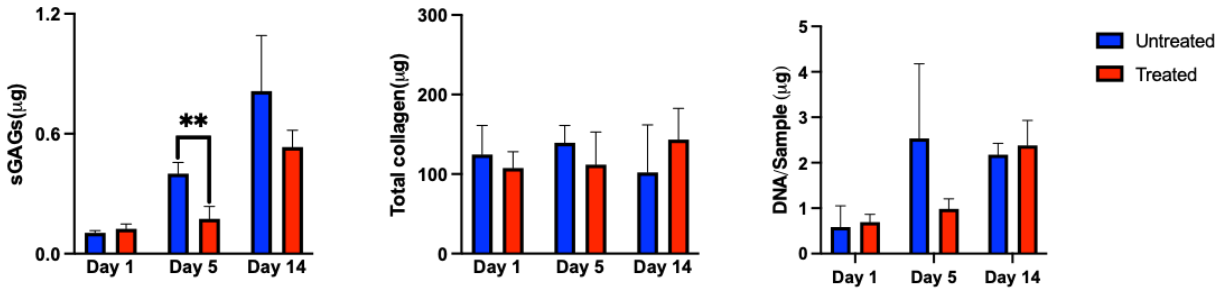

*Figure 12: Biochemical quantification of extracellular matrix components and cellular content in spheroids across Day 1, Day 5 and Day 14 for C-ABC treated and untreated conditions. *p<0.05, **p<0.01, ***p<0.001, ****p<0.0001*

3.3.3. C-ABC Treatment on PRG4+ Spheroids

To study the effect of C-ABC at early time points, the treatment was performed either 24h or 5 days post media change.

3.3.3.1. Day 1 treated spheroids

25 spheroids were treated with C-ABC at Day 1, and 30 spheroids were used as control for 4 hours at 37℃ and 5% CO_2. Spheroids were imaged for 5 timepoints (0h, 24h, 25h, 26h and 27h) before the treatment and 4 timepoints after the treatment (31h, 32h, 33h and 34h).

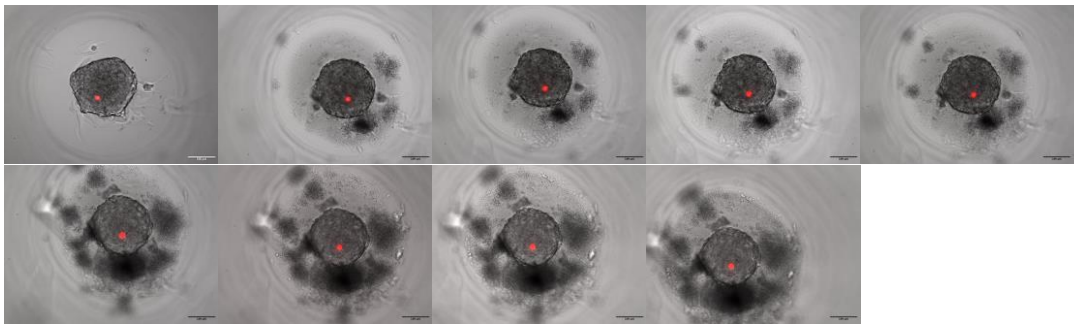

Figure 13: Representative imaging of PRG4+ spheroids containing sensors tracked treated at 27th h. (Top left to right: Day 0 to 27h, Bottom left to right:31h to 34h)

3.3.3.2. Microenvironmental mechanical parameter changes for Day 1 treated spheroids

Changes in mechanical parameters like average pressure, elastic energy density and volume for the sensors were measured to evaluate the effect of C-ABC treatment on the mechanical microenvironment of PRG4+ spheroids. Overall changes in the mechanical parameters were assessed over time and just before and after the treatment. Additionally, individual sensors were tracked to analyze individual trends in sensor's parameters pre- and post-treatment. Finally, sensors were distinguished based on their location within spheroid, specifically core and shell regions, to determine whether treatment-induced mechanical responses varied by positions.

A. Mean mechanical parameters

Mean mechanical parameters were calculated by averaging values for each parameter at each timepoint and plotted over time (*Figure 14*). This approach provided and overall trend in the mechanical microenvironment within spheroids. No significant change in mean average pressure, mean volume or mean elastic energy density was observed at any given timepoints and between control and treatment groups.

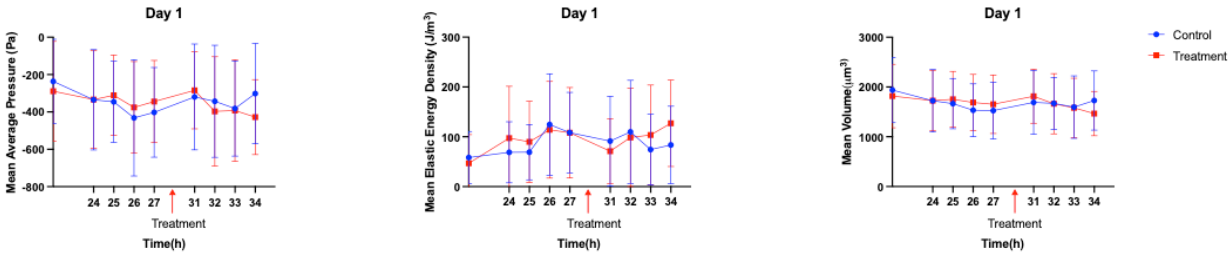

Figure 14: Mean average pressure (Pa), Mean elastic energy density (J/m^3) and Mean volume (μm^3) in Day 1 treated spheroids plotted over time.

Mean mechanical parameters were also compared pre-and post-treatment on Day 1. No significant change was observed. Additionally, mean mechanical parameters were compared immediately pre- and post-treatment C-ABC treatment on Day 1 to assess the immediate response of mechanical microenvironment. No significant changes were observed in any parameters for both control and C-ABC treated groups.

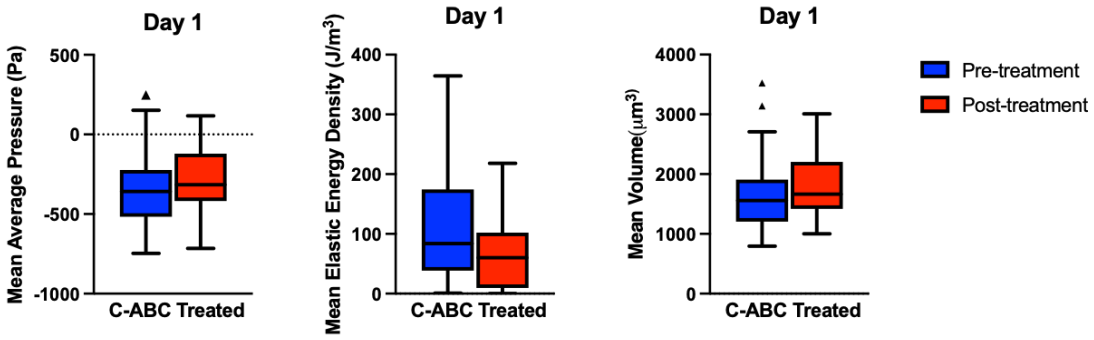

Figure 15: Mean average pressure (Pa), Mean elastic energy density (J/m^3) and Mean volume (μm^3) in Day 1 treated spheroids right pre- and post-treatment.

B. Parameters by individual sensor

Figure 16 shows mechanical parameters for individual sensors pre- and post C-ABC treatment on Day 1. To assess changes in mechanical parameters for individual sensors, percentage change in each parameter was calculated. No clear increase or decrease trends could be observed.

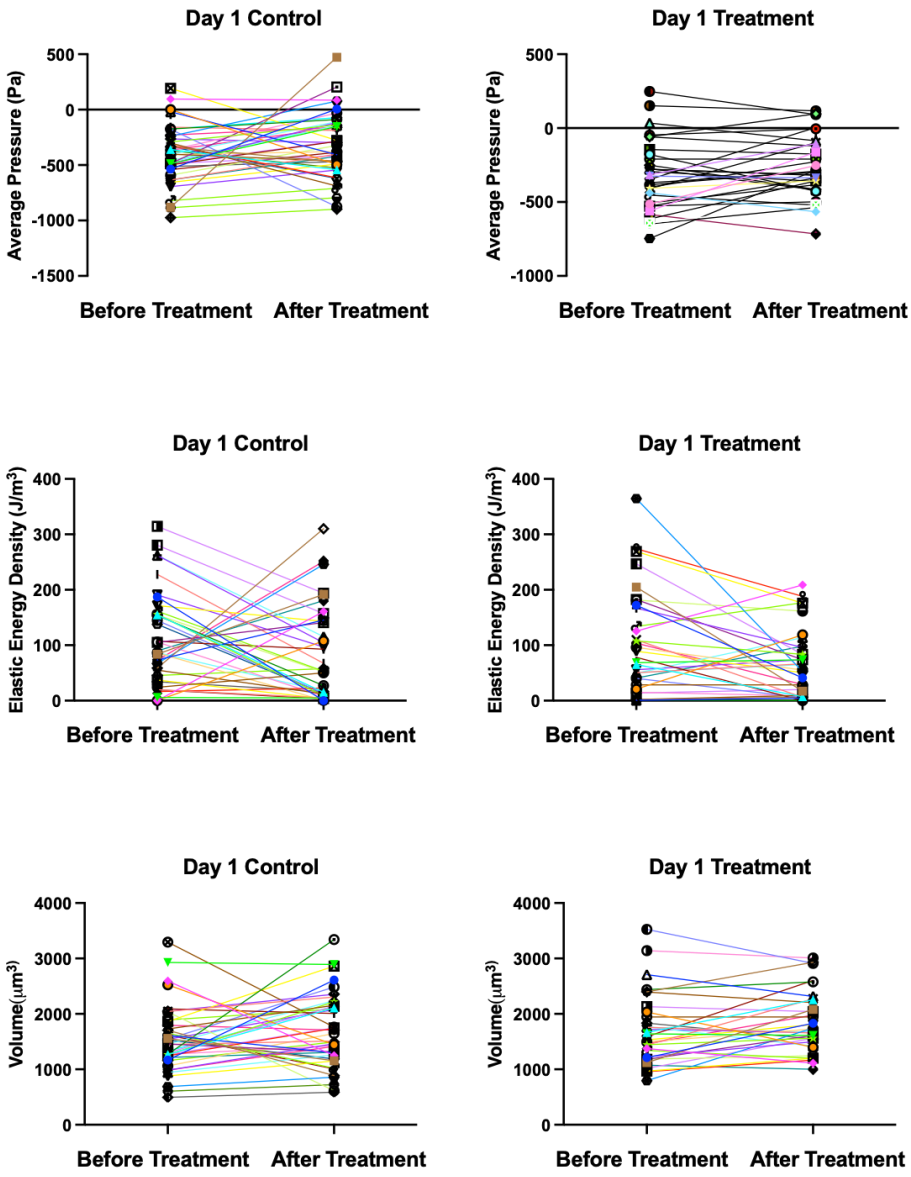

Figure 16: Average pressure (Pa), Mean elastic energy density (J/m^3) and Mean volume (μm^3) for individual sensor pre- and post-treatment.

C. Parameters by region

Sensor position within the spheroid can influence the mechanical pressure and forces it experiences. To evaluate this, the spheroid was partitioned into core and shell regions, with the core defined as the central 50% of the total volume and the rest outer volume designated as the shell. Sensors were segregated based on their location within spheroid, and the mechanical parameters were quantified pre- and post-treatment to assess the region-dependent differences. N = 8 spheroids were assessed for each region. Region-specific change in mechanical parameters pre and post treatment was non-significant in both control (*Figure B.3*) and treatment group (*Figure 17*).

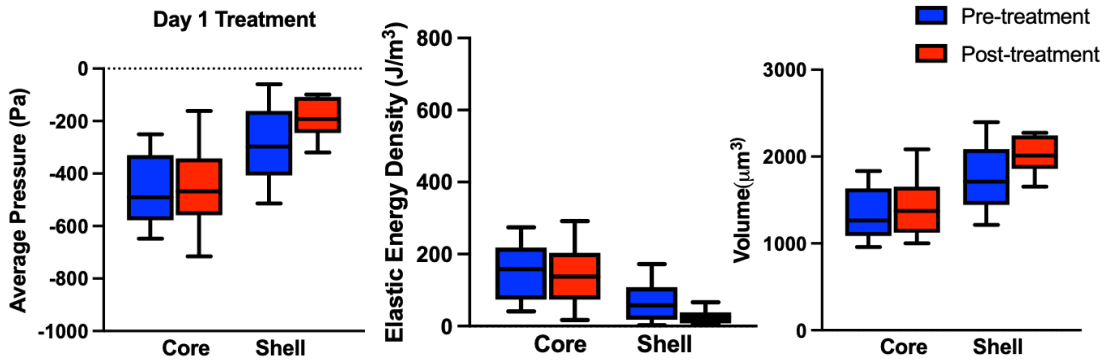

Figure 17: Average pressure (Pa), Elastic energy density (J/m^3) and Volume (μm^3) in Day 1 treated spheroids right pre- and post-treatment in core and shell regions.

3.3.3.3. Day 5 treated spheroid

32 spheroids were treated with C-ABC at Day 5 and 33 spheroids were used as control for 4 hours at 37℃ and 5% CO_2. Spheroids were imaged for 6 timepoints (Day 0, 1, 2, 3, 4 and 5) before the treatment and 4 timepoints after the treatment (Day 5, 6, 7 and 8).

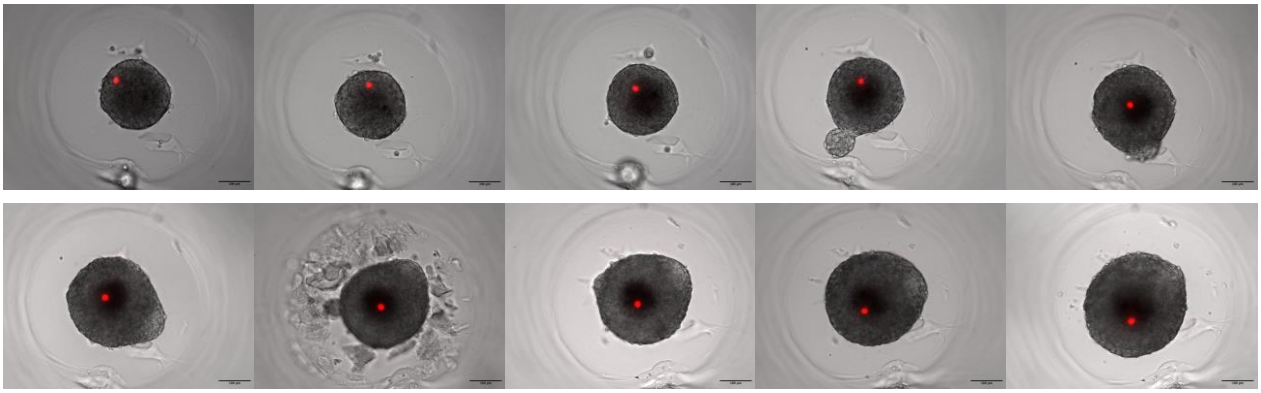

Figure 18: Representative imaging of PRG4+ spheroids containing sensors tracked treated at Day 5. (Top left to right: Day 0 to Day 4, Bottom left to right: Day 5 before treatment to Day 10)

3.3.3.4. Microenvironmental mechanical parameter changes for Day 5 treated spheroids

Average pressure, elastic energy density and volume for the sensors were measured to assess the changes in mechanical environment upon C-ABC treatment on the mechanical microenvironment of PRG4+ spheroids. Overall changes in the mechanical parameters were assessed over time and just before and after the treatment. Additionally, individual sensors were tracked to analyze individual trends in sensor's parameters pre- and post-treatment. Finally, sensors were distinguished based on their location within spheroid, specifically core and shell regions, to determine whether treatment-induced mechanical responses varied by regions.

A. Mean mechanical parameters

Figure 19 shows changes in mechanical parameters for Day 5 treated spheroids over the period.

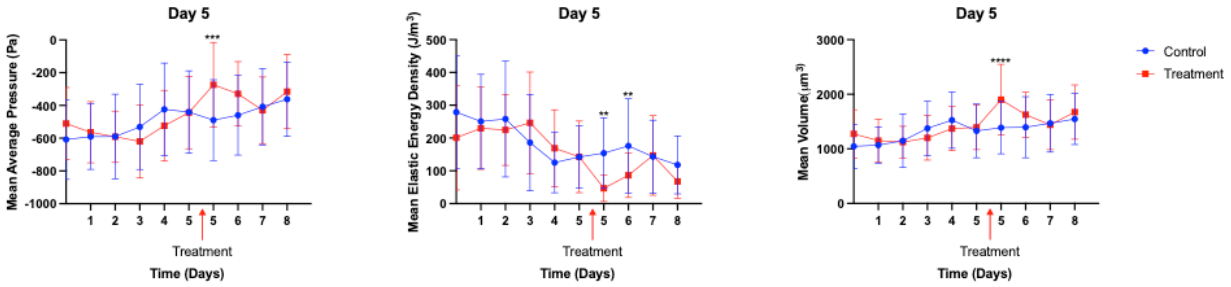

*Figure 19: Mean average pressure (Pa), Mean elastic energy density (J/m^3) and Mean volume (µm^3) in Day 5 treated spheroids plotted over time. . *p<0.05, **p<0.01, ***p<0.001,*

Significant decrease in mean average pressure was observed in treatment group after C-ABC treatment compared to before (p=0.0012) as well as compared to control group (p=0.0069). *Figure 20* shows changes in mean average pressure, mean elastic energy density and mean volume of the force sensors before and after C-ABC treatment.

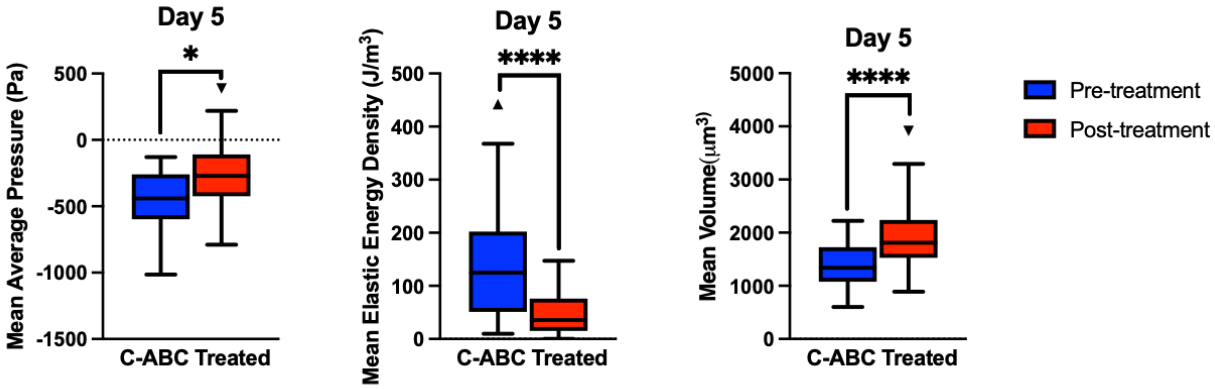

*Figure 20: Mean average pressure (Pa), Mean elastic energy density (J/m^3) and Mean volume (µm^3) in Day 5 treated spheroids pre- and post-treatment. *p<0.05, **p<0.01, ***p<0.001, ****p<0.0001*

Similarly, mean elastic energy decreased post treatment for C-ABC treated compared to both before treatment ($p<0.0001$) as well as control ($p<0.0001$). Mean volume of the sensors post treatment for C-ABC treated group was significantly higher than pretreatment group ($p<0.0001$) as well as control group ($p<0.0001$). No changes in the mechanical parameters were observed in the control group (*Figure B.4*).

B. Parameters by individual sensor

Figure 21 shows changes in average pressure, elastic energy and volume of each sensor pre- and post-treatment. A clear trend of increasing average pressure and volume and decreasing elastic energy density could be seen. Percentage change was calculated for each sensor and parameter. Average pressure after treatment was decreasing by $27\pm38\%$ ($p=0.012$) compared to before treatment, volume was found to be increasing by $32\pm50\%$ ($p<0.0001$) treatment respectively. Similarly, elastic energy density was increased by $62\pm33\%$ ($p<0.0001$) compared to pretreatment.

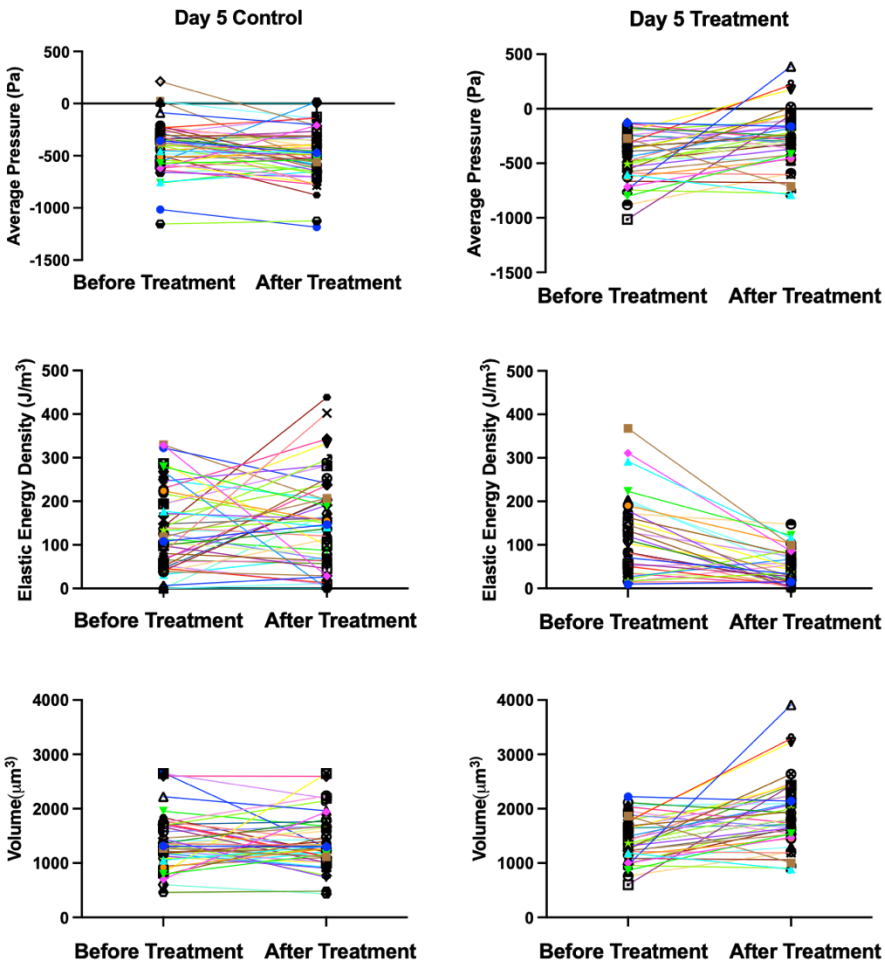

Figure 21: Average pressure (Pa), Mean elastic energy density (J/m^3) and Mean volume (μm^3) for individual sensor pre- and post- treatment.

C. Parameters by region

Sensor position within the spheroid can influence the mechanical pressure and forces it experience. To evaluate this, the spheroid was partitioned into core and shell regions, with the core defined as the central 50% of the total volume and the rest outer volume designated as the shell. Sensors were segregated based on their location within spheroid at Day 4, and the mechanical parameters were quantified pre- and post-treatment to assess the region-dependent

differences. N = 8 spheroids were assessed for each region. Shell region of the spheroids was found to have lower average pressure (p=0.0031) and elastic energy density (p=0.0008), and higher volume (p=0.0039) compared to core region after C-ABC treatment (*Figure 22*).

Average pressure in core (p=0.0010) and shell (p=0.0011) region decreased after C-ABC treatment. Elastic energy density after C-ABC treatment decreased significantly in both core (p=0.0008) and shell (p=0.0295) regions. Additionally, volume of the sensors post treatment increased significantly in core (p=0.0051) and shell (p<0.0001) regions. No changes in the mechanical parameters for core and shell region pre- and post-treatment were observed in the control group (*Figure B.5*).

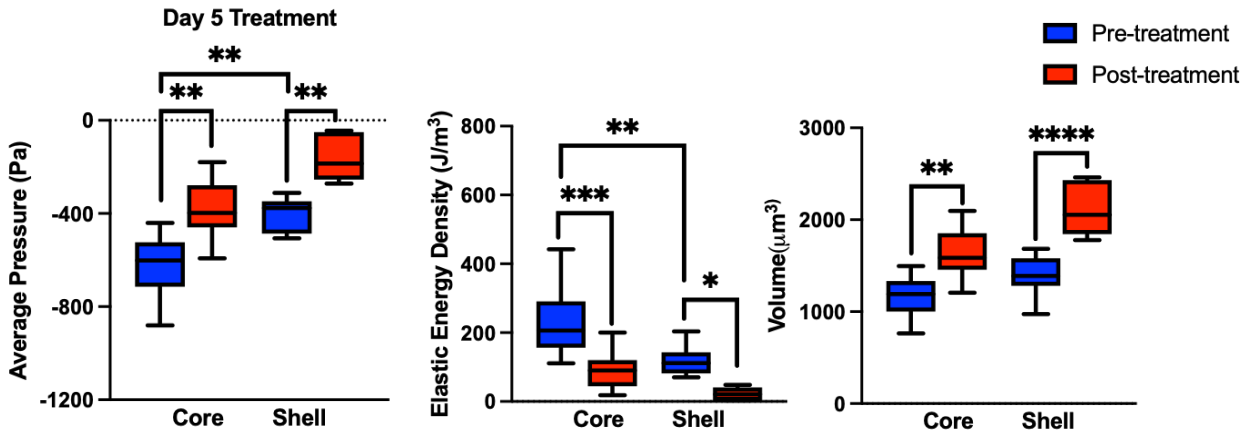

*Figure 22: Average pressure (Pa), Elastic energy density (J/m^3) and Volume (μm^3) in Day 5 treated spheroids right pre- and post-treatment in core and shell regions. *p<0.05, **p<0.01, ***p<0.001, ****p<0.0001*

3.4. Discussion

The study aimed to quantify changes in microenvironmental forces in a chondrogenic spheroid model upon matrix degradation. Two timepoints were analyzed to assess these changes: Day 1 and Day 5 of spheroids in chondrogenic culture. No significant changes were observed in mechanical parameters of sensors for Day 1 treated spheroids (*Figure 14 and 15*). This can be attributed to relatively low amounts of GAGs at Day 1, as confirmed by the DMMB assay (*Figure 12*), indicating non-sufficient presence of sGAGs in the ECM to generate measurable mechanical changes upon degradation. Additionally, the sensors may still be undergoing stabilization, resulting in increased variability to treatment induced changes.

On the other hand, significant changes were observed in Day 5 treated spheroids. A decrease in mean average pressure and elastic energy density, along with corresponding increase in sensor volume was measured post treatment (*Figure 19 and 20*). This is consistent with the reduction in compressive forces, lowering the pressure exerted on them and thereby, allowing the sensor to partially recover their undeformed state. These observations are supported by the DMMB assay for Day 5 spheroids, which showed a significant decrease in GAG content following C-ABC treatment (*Figure 12*). These results highlight the role of GAGs in establishing a compressive resilience microenvironment in cartilage tissues.

Importantly, the findings also suggested that mean mechanical parameters alone might be insufficient to fully interpret the observations. While averaged values suggest that the treatment does reduce the microenvironmental forces, the high variability across the measurements suggests the need to investigate changes individual sensors pre- and post-treatment. Percentage change in mechanical parameter by tracking individual sensors for Day

5 treated spheroids further confirmed the hypothesis (*Figure 21*). Whereas no significant percentage change was found in Day 1 treated spheroids (*Figure 16*).

Another reason for the high variability in the average values could be described based on the placement of the sensors within the spheroid. As the outer shell region is more directly exposed to the surrounding medium and may experience greater nutrient availability, diffusion of treatment molecules, and dynamic cellular activity. In contrast, the core region is more confined and may be subjected to limited diffusion, increased cell density, and mechanical constraints. Sensors located in the core and shell regions exhibited differences in mechanical parameters, indicating that the position within spheroid influences forces experienced having high average pressure within core than shell regions for Day 5 treated spheroids (*Figure 22*). Day 1 on the other hand had no significant change in mechanical parameters across the regions (*Figure 17*).

The observed decrease in compressive forces, accompanied by an increase in sensor volume, reflects a release of ECM-induced mechanical constraints. This relationship suggests that ECM particularly GAGs play a dominant role in maintaining compressive pressure within the spheroid, and that its degradation leads to partial relaxation in the microenvironment. Such findings are consistent with the known role of GAGs in compression and maintaining tissue hydration, further supporting the link between biochemical composition and mechanical function[34-36].

One limitation of this study could be the inaccuracies in the image processing software, as it sometimes does overanalyze or under analyze the sensors based on the Otsu detection thresholds. This could lead to high variability and large error bars, potentially obscuring subtle

trends. Additionally, the distribution of sensor within spheroid is not uniform, majority of it reside in the core, this could result in biased representation of the regions.

Future work could explore the changes in microenvironmental forces with treatment at later timepoints (t = 10^{th} day or 14^{th} day). Along with that, additional enzymes could also be evaluated to determine whether similar trends are observed across different modes of matrix disruption. For instance, collagenase could be used to selectively degrade collagen within the spheroid and assess how alterations in collagen network influence microenvironmental forces. Extending this approach to multiple matrix components would provide a more comprehensive understanding of how different extracellular matrix constituents might contribute to the mechanical microenvironment. Such insights could be particularly valuable in the context of osteoarthritis, where both GAGs and collagen degradation play critical role in disease progression[42-43]. This platform therefore has the potential to serve as 3D *in vitro* model to study disease-associated mechanical changes. Additionally, this system may have applications in tissue engineering by enabling the study of how enzymatic modulation of the matrix influences mechanical stability within developing cartilage constructs[44-45]. Understanding the role of treatments such as C-ABC in altering microenvironmental forces and thereby, informing strategies to engineer cartilage with improved structural and functional properties.

Overall, this study provides a robust approach to quantify changes in the mechanical microenvironment within chondrogenic spheroids. It extends the understanding of GAG degradation by demonstrating how such degradation translates into measurable changes.

CHAPTER 4:

CONCLUSION

Microenvironmental forces play a critical role in regulating cell behavior, including motility, viability, proliferation, and apoptosis[1-2]. These forces have been extensively studied in 2D cell systems due to their experimental accessibility and controllability[10-11]. However, such systems fail to fully recapitulate the structural and mechanical complexity of native tissues. This limitation highlights the need for physiologically relevant *in vitro* systems than enable quantification of mechanical forces within 3D microenvironments.

In this study, HCMPs were used to investigate how microenvironmental forces evolve under different structural and matrix conditions using two models: dog bone system and chondrogenic spheroid model subjected to matrix degradation. Together, these models provide a framework for understanding the role of ECM composition and cell-cell interaction in modulating mechanical microenvironments.

The findings suggest that cellular interactions alone are capable of generating microenvironmental forces. However, in the absence of a well-developed extracellular matrix, these forces are limited in magnitude and exhibit high variability. This indicates that while cells contribute to the generation of mechanical forces, the lack of structured matrix restricts the ability of these forces to accumulate and be consistently measured. In contrast, the spheroid model demonstrates that once sufficiently developed matrix is present, mechanical forces become more structured.

Importantly, this study reveals that the degradation of GAGs alters the mechanical microenvironment by relieving compressive pressure and allowing local relaxation of forces. This suggests that the ECM functions as both a structural scaffold and a mechanical reservoir.

The insights from this work have brought implication for both disease, modeling and engineering. In the context of disease, such as osteoarthritis, where progressive degradation of ECM components alters tissue mechanics, this platform provides a means to directly link biochemical changes to mechanical outcomes. Similarly, tissue, engineering application, understanding how matrix composition, regulates, mechanical cues can inform strategies to design constructs with improved functional properties and structural integrity.

Overall, this study demonstrates that microenvironmental forces in 3D systems arise from both cellular and ECM interactions.

Appendix

A. Dog bone microtissue

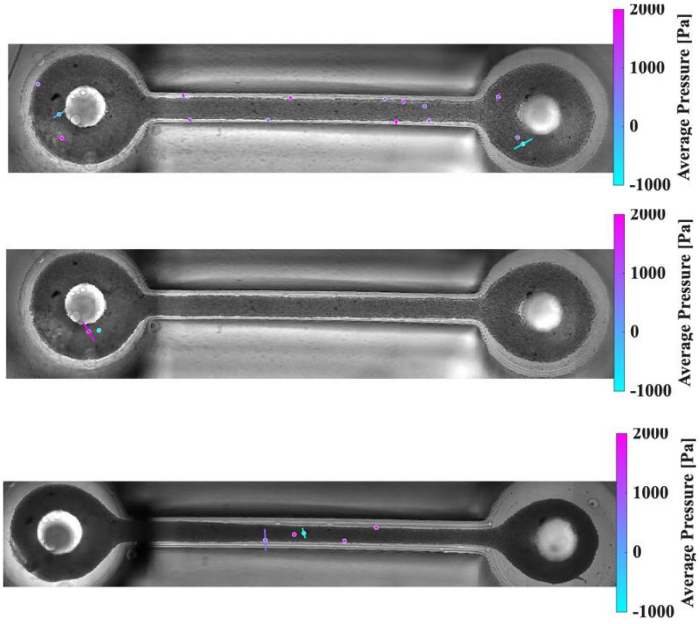

Figure A.1.: Brightfield images of one representative NHF-seeded dog bone microtissue at 4h, 8h, 24h with overlayed map of sensor locations, average pressure, and elongation. For each sensor, color corresponds to average pressure magnitude (Pa), length of arrows corresponds to elongation, and direction of arrow corresponds to major axis.

B. Spheroid microtissue

Figure B.1.: Agarose mold for 96 well plate and 24 well plate microarray

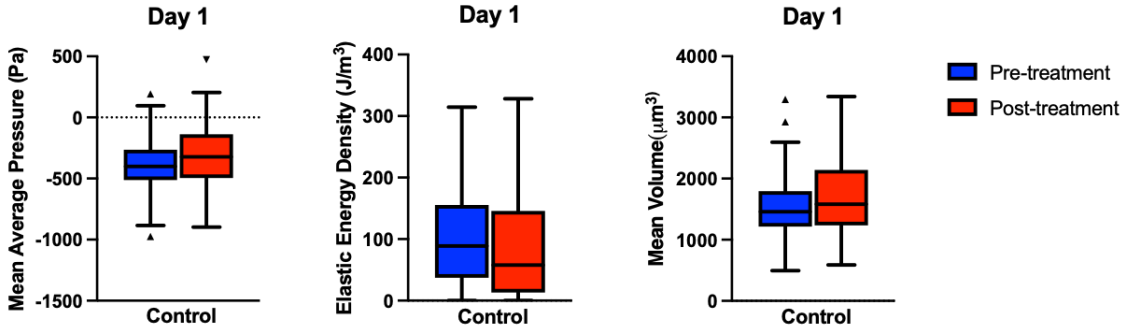

Figure B.2.: Mean average pressure (Pa), Mean elastic energy density (J/m^3) and Mean volume (µm^3) in Day 1 control spheroids pre- and post-treatment.

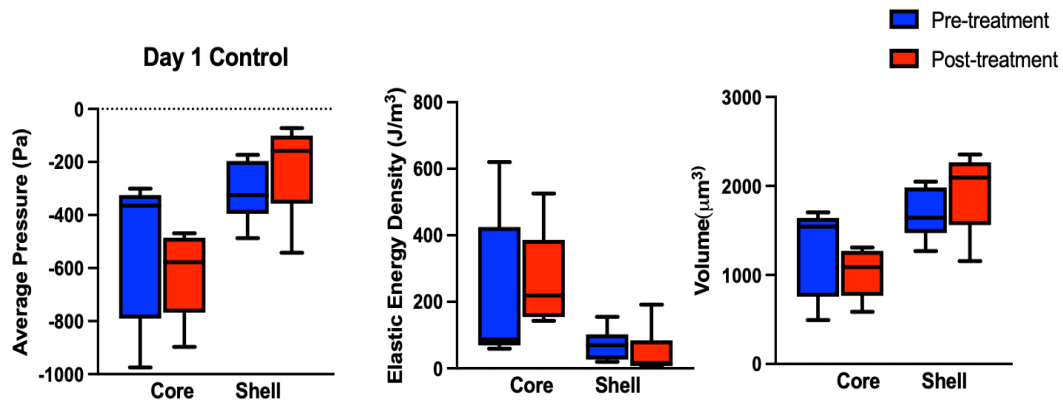

Figure B.3: Average pressure (Pa), Elastic energy density (J/m^3) and Volume (µm^3) in Day 1 control spheroids pre-and post-treatment in core and shell regions.

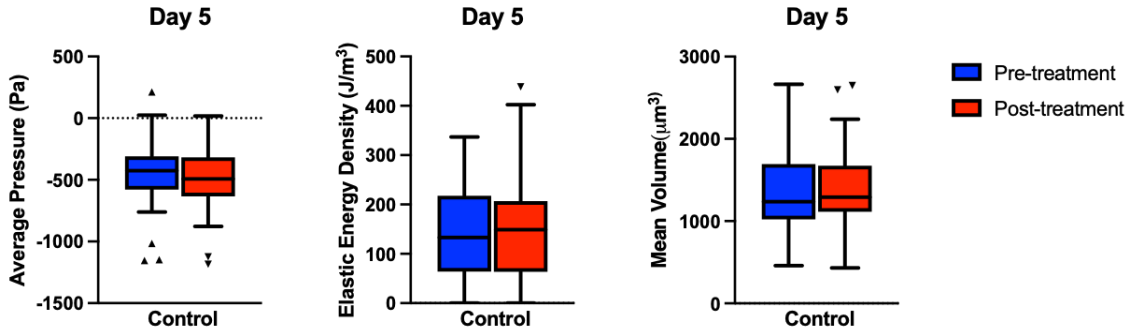

Figure B.4: Mean average pressure (Pa), Mean elastic energy density (J/m^3) and Mean volume (μm^3) in Day 5 control spheroids pre- and post-treatment.

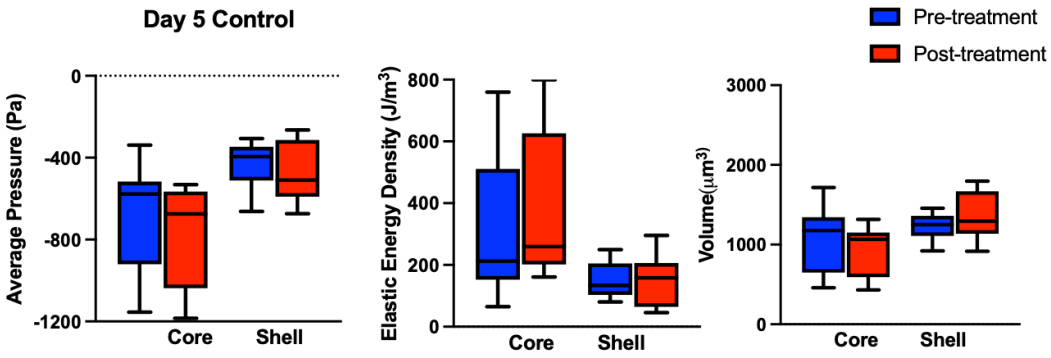

Figure B.5: Average pressure (Pa), Elastic energy density (J/m^3) and Volume (μm^3) in Day 5 control spheroids pre-and post-treatment in core and shell regions.

References

1. Lecuit, T., & Lenne, P. F. (2007). Cell surface mechanics and the control of cell shape, tissue patterns and morphogenesis. *Nature reviews Molecular cell biology*, *8*(8), 633-644.
2. Mammoto, T., & Ingber, D. E. (2010). Mechanical control of tissue and organ development. *Development*, *137*(9), 1407-1420.
3. Schwartz, M. A. (2010). Integrins and extracellular matrix in mechanotransduction. *Cold Spring Harbor perspectives in biology*, *2*(12), a005066.
4. Mierke, C. T. (2024). Extracellular matrix cues regulate mechanosensing and mechanotransduction of cancer cells. *Cells*, *13*(1), 96.
5. Moeendarbary, E., & Harris, A. R. (2014). Cell mechanics: principles, practices, and prospects. *Wiley Interdisciplinary Reviews: Systems Biology and Medicine*, *6*(5), 371-388.
6. Bai, M., Cai, L., Li, X., Ye, L., & Xie, J. (2020). Stiffness and topography of biomaterials dictate cell-matrix interaction in musculoskeletal cells at the bio-interface: a concise progress review. *Journal of Biomedical Materials Research Part B: Applied Biomaterials*, *108*(6), 2426-2440.
7. Su, F. C., Wu, C. C., & Chien, S. (2011). Roles of microenvironment and mechanical forces in cell and tissue remodeling. *J Med Biol Eng*, *31*, 233-244.
8. Ghosh, K., & Ingber, D. E. (2007). Micromechanical control of cell and tissue development: implications for tissue engineering. *Advanced drug delivery reviews*, *59*(13), 1306-1318.
9. Agha, R., Ogawa, R., Pietramaggiori, G., & Orgill, D. P. (2011). A review of the role of mechanical forces in cutaneous wound healing. *Journal of Surgical Research*, *171*(2), 700-708.
10. Dembo, M., Oliver, T., Ishihara, A., & Jacobson, K. (1996). Imaging the traction stresses exerted by locomoting cells with the elastic substratum method. *Biophysical journal*, *70*(4), 2008-2022.
11. Legant, W. R., Miller, J. S., Blakely, B. L., Cohen, D. M., Genin, G. M., & Chen, C. S. (2010). Measurement of mechanical tractions exerted by cells in three-dimensional matrices. *Nature methods*, *7*(12), 969-971.
12. Tan, J. L., Tien, J., Pirone, D. M., Gray, D. S., Bhadriraju, K., & Chen, C. S. (2003). Cells lying on a bed of microneedles: an approach to isolate mechanical force. *Proceedings of the National Academy of Sciences*, *100*(4), 1484-1489.
13. Hwang, H., Kim, Y., Park, J. H., & Jeong, U. (2020). 2D percolation design with conductive microparticles for low-strain detection in a stretchable sensor. *Advanced Functional Materials*, *30*(13), 1908514.
14. Gutierrez, R. A., Fang, W., Kesari, H., & Darling, E. M. (2021). Force sensors for measuring microenvironmental forces during mesenchymal condensation. *Biomaterials*, *270*, 120684.

15. Rodriguez Navas, M., & Darling, E. M. (2025). Selection of force sensors for in situ measurement of neotissue microenvironments. *Tissue Engineering Part A*, *31*(3-4), 164-173.
16. Kjaer, M. (2004). Role of extracellular matrix in adaptation of tendon and skeletal muscle to mechanical loading. *Physiological reviews*.
17. Bramson, M. T., Van Houten, S. K., & Corr, D. T. (2021). Mechanobiology in tendon, ligament, and skeletal muscle tissue engineering. *Journal of Biomechanical Engineering*, *143*(7), 070801.
18. Bourget, J. M., Guillemette, M., Veres, T., Auger, F. A., & Germain, L. (2013). Alignment of cells and extracellular matrix within tissue-engineered substitutes. *Advances in biomaterials science and biomedical applications*, 365-390.
19. Sarasa-Renedo, A., & Chiquet, M. (2005). Mechanical signals regulating extracellular matrix gene expression in fibroblasts. *Scandinavian journal of medicine & science in sports*, *15*(4), 223-230.
20. Schell, J. Y., Wilks, B. T., Patel, M., Franck, C., Chalivendra, V., Cao, X., ... & Morgan, J. R. (2016). Harnessing cellular-derived forces in self-assembled microtissues to control the synthesis and alignment of ECM. *Biomaterials*, *77*, 120-129.
21. Tour, G., Wendel, M., & Tcacencu, I. (2013). Human fibroblast-derived extracellular matrix constructs for bone tissue engineering applications. *Journal of Biomedical Materials Research Part A*, *101*(10), 2826-2837.
22. Dubay, R., Darling, E. M., & Fiering, J. (2023). Microparticles with tunable, cell-like properties for quantitative acoustic mechanophenotyping. *Microsystems & Nanoengineering*, *9*(1), 90.
23. Dubay, R., Fiering, J., & Darling, E. M. (2020). Effect of elastic modulus on inertial displacement of cell-like particles in microchannels. *Biomicrofluidics*, *14*(4).
24. Darling, E. M., Zauscher, S., & Guilak, F. (2006). Viscoelastic properties of zonal articular chondrocytes measured by atomic force microscopy. *Osteoarthritis and cartilage*, *14*(6), 571-579.
25. Ma, X., Schickel, M. E., Stevenson, M. D., Sarang-Sieminski, A. L., Gooch, K. J., Ghadiali, S. N., & Hart, R. T. (2013). Fibers in the extracellular matrix enable long-range stress transmission between cells. *Biophysical journal*, *104*(7), 1410-1418.
26. Pandya, P., Orgaz, J. L., & Sanz-Moreno, V. (2017). Actomyosin contractility and collective migration: may the force be with you. *Current opinion in cell biology*, *48*, 87-96
27. Pincha, N., Saha, D., Bhatt, T., Zirmire, R. K., & Jamora, C. (2018). Activation of fibroblast contractility via cell-cell interactions and soluble signals. *Bio-protocol*, *8*(18), e3021-e3021.
28. Akkiraju, H., & Nohe, A. (2015). Role of chondrocytes in cartilage formation, progression of osteoarthritis and cartilage regeneration. *Journal of developmental biology*, *3*(4), 177-192.

29. Gordon, E., Schimmel, L., & Frye, M. (2020). The importance of mechanical forces for in vitro endothelial cell biology. *Frontiers in Physiology*, *11*, 684.
30. Gaut, C., & Sugaya, K. (2015). Critical review on the physical and mechanical factors involved in tissue engineering of cartilage. *Regenerative medicine*, *10*(5), 665-679.
31. Statham, P., Jones, E., Jennings, L. M., & Fermor, H. L. (2022). Reproducing the biomechanical environment of the chondrocyte for cartilage tissue engineering. *Tissue Engineering Part B: Reviews*, *28*(2), 405-420.
32. Steinert, A. F., Ghivizzani, S. C., Rethwilm, A., Tuan, R. S., Evans, C. H., & Nöth, U. (2007). Major biological obstacles for persistent cell-based regeneration of articular cartilage. *Arthritis research & therapy*, *9*(3), 213.
33. Vincent, T. L., & Wann, A. K. (2019). Mechanoadaptation: articular cartilage through thick and thin. *The Journal of physiology*, *597*(5), 1271-1281.
34. Horkay, F., Douglas, J. F., & Raghavan, S. R. (2021). Rheological properties of cartilage glycosaminoglycans and proteoglycans. *Macromolecules*, *54*(5), 2316-2324.
35. Gilbert, S. J., Bonnet, C. S., & Blain, E. J. (2021). Mechanical cues: bidirectional reciprocity in the extracellular matrix drives mechano-signalling in articular cartilage. *International journal of molecular sciences*, *22*(24), 13595.
36. Baylon, E. G., & Levenston, M. E. (2020). Osmotic Swelling Responses Are Conserved Across Cartilaginous Tissues With Varied Sulfated-Glycosaminoglycan Contents. *Journal of Orthopaedic Research®*, *38*(4), 785-792.
37. MacBarb, R. F., Makris, E. A., Hu, J. C., & Athanasiou, K. A. (2013). A chondroitinase-ABC and TGF-β1 treatment regimen for enhancing the mechanical properties of tissue-engineered fibrocartilage. *Acta biomaterialia*, *9*(1), 4626-4634.
38. Natoli, R. M., Revell, C. M., & Athanasiou, K. A. (2009). Chondroitinase ABC treatment results in greater tensile properties of self-assembled tissue-engineered articular cartilage. *Tissue Engineering Part A*, *15*(10), 3119-3128.
39. Huey, D. J., & Athanasiou, K. A. (2011). Maturational growth of self-assembled, functional menisci as a result of TGF-β1 and enzymatic chondroitinase-ABC stimulation. *Biomaterials*, *32*(8), 2052-2058.
40. Responte, D. J., Arzi, B., Natoli, R. M., Hu, J. C., & Athanasiou, K. A. (2012). Mechanisms underlying the synergistic enhancement of self-assembled neocartilage treated with chondroitinase-ABC and TGF-β1. *Biomaterials*, *33*(11), 3187-3194.
41. Kozhemyakina, E., Zhang, M., Ionescu, A., Ayturk, U. M., Ono, N., Kobayashi, A., ... & Lassar, A. B. (2015). Identification of a Prg4-expressing articular cartilage progenitor cell population in mice. *Arthritis & rheumatology*, *67*(5), 1261-1273
42. Gauci, S. J., Stanton, H., Little, C. B., & Fosang, A. J. (2017). Proteoglycan and collagen degradation in osteoarthritis. *Cartilage: Volume 2: Pathophysiology*, 41-61.
43. Poole, A. R., Kobayashi, M., Yasuda, T., Laverty, S., Mwale, F., Kojima, T., ... & Wu, W. (2002). Type II collagen degradation and its regulation in articular cartilage in osteoarthritis. *Annals of the rheumatic diseases*, *61*(suppl 2), ii78-ii81.

44. Williams, G. M., Lin, J. W., & Sah, R. L. (2007). Cartilage reshaping via in vitro mechanical loading. *Tissue engineering*, *13*(12), 2903-2911.
45. Ng, K. W., Kugler, L. E., Doty, S. B., Ateshian, G. A., & Hung, C. T. (2009). Scaffold degradation elevates the collagen content and dynamic compressive modulus in engineered articular cartilage. *Osteoarthritis and cartilage*, *17*(2), 220-227